Electronic Supplementary Material (ESI) for Journal of Materials Chemistry A.

Supporting Information: Investigating structural properties and reaction mechanism of non-stoichiometric spinel LNMO via solid state NMR

Nahom Enkubahri Asres,[†,‡] Naiara Etxebarria,[†] Iciar Monterrubio,[†,‡] Damien Saurel,[†] Christian Fink Elkjær,[¶] Montse Casas-Cabanas,[†,§] Marine Reynaud,[†] Marcus Fehse,[*,†] and Juan Miguel López del Amo[*,†]

†*Center for Cooperative Research on Alternative Energies (CIC energiGUNE), Basque Research and Technology Alliance (BRTA), Alava Technology Park, Albert Einstein 48, 01510, Vitoria-Gasteiz, Spain*

‡*Department of Organic and Inorganic Chemistry, Faculty of Science and Technology, University of the Basque Country, UPV/EHU,Bº Sarriena s/n, 48940 Leioa, Spain*

¶*Haldor A/S, Haldor Topsøes Allé 1, 2800 Kgs. Lyngby, Denmark*

§*Ikerbasque - Basque Foundation for Science, Maria Diaz de Haro 3, 48013 Bilbao, Spain*

E-mail: marcus.fehse@umontpellier.fr; jmlopez@cicenergigune.com

Magnetic measurements The AC magnetic susceptibility and Magnetisation versus DC magnetic field at 5 K are presented in Fig. S1. According to [S1], and assuming spin only contribution to the magnetic moment (i.e. quenched orbital moment or infinite crystalline field) the magnetisation at saturation has the following dependency on the excess y of Mn:[S1, S2]

$$M_{sat} = g((1.5 - y)S_{Mn^{IV}} - (0.5 - y)S_{Ni^{II}} - 2yS_{Mn^{III}}) \tag{1}$$

Where $S_{Mn^{IV}} = 1.5$, $S_{Ni^{II}} = 1$ and $S_{Mn^{III}} = 2$. The excess Mn y can hence be calculated as:

$$y = \frac{3.5 - M_{sat}}{9} \tag{2}$$

The Mn^{3+} content $2y$ calculated from magnetisation at saturation from eq. 2, and Curie temperature of LNMO-O-45 and LNMO-O-48 determined from Fig. S1 are compared in Fig. 1(c) in the main manuscript.

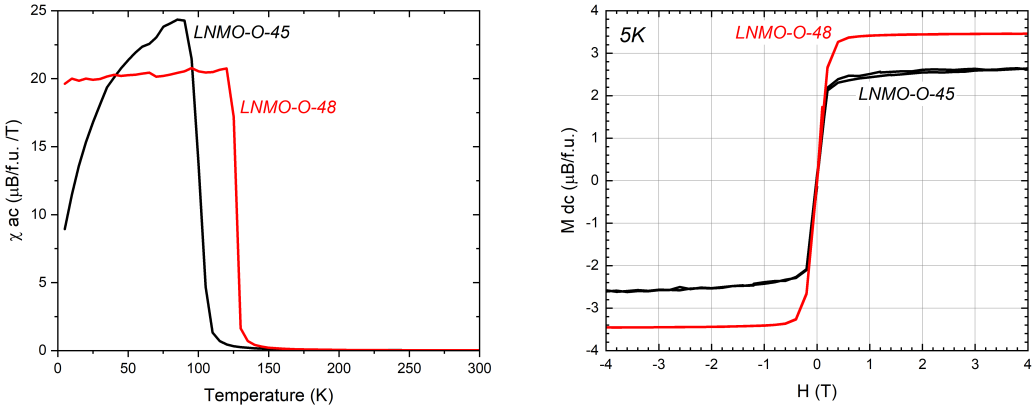

Figure S1: AC magnetic susceptibility versus temperature (left panel) and Magnetisation versus DC magnetic field at 5 K (right panel) of LNMO-O-45 and LNMO-O-48.

SEM Micrographs of secondary electron microscopy of the LNMO-O-45 and LNMO-O-48 are compared in Fig. S2 left and right, respectively. The images reveal that both samples are composed of secondary spherical particles with an average diameter of $\approx 8\mu$m. The spherical secondary particles are composed of smaller primary polygonal shaped particles with dimension in the range of 1.5 μm.

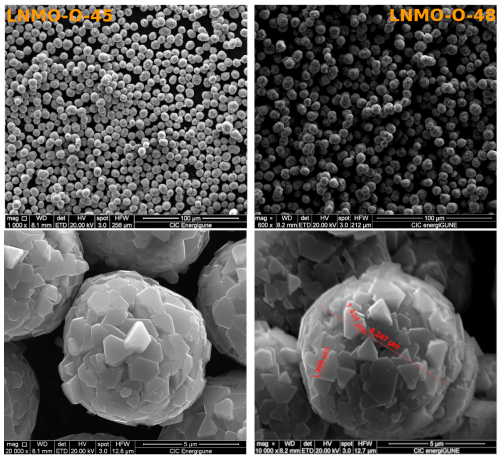

Figure S2: SEM micrographs of LNMO-O-45 (left) and LNMO-O-48 (right) at different at low (top) and high (bottom) magnification.

NMR In Fig S3, the complete ^{7}Li NMR spectra of TM ordered near stoichiometric (LNMO-O-48) and non stoichiometric LNMO-O-45 are presented. The rotational side bands are indicated by star markers. It is salient that almost negligible diamagnetic Li containing species such as LiOH or Li_2Co_3 (expected signal around 0 ppm) are present in these materials, confirming their purity.

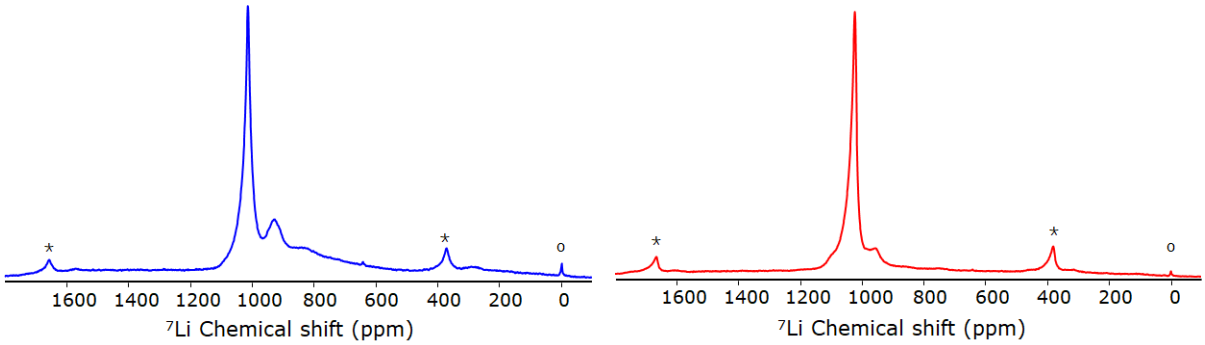

Figure S3: ^{7}Li NMR spectra of pristine near stoichiometric LNMO-O-48 (right) and non-stoichiometric LNMO-O-45 (left) TM ordered LNMO samples.

Peak intensity (Int.), chemical shift (shift) and linewidth (LW) for the 4 components identified in *ex situ* ^{7}Li NMR during charge and discharge at distinct SOC (x in Li_xNMO) are summarised in Tab. S1.

Table S1: Peak intensity of deconvoluted ^{7}Li NMR spectra for LNMO-45 at distinct SOC

SOC / Comp	x = 0.7 Int. [%]	shift [ppm]	LW [ppm]	x = 0.6 Int. [%]	shift [ppm]	LW [ppm]	x = 0.5 Int. [%]	shift [ppm]	LW [ppm]	x = 0.4 Int. [%]	shift [ppm]	LW [ppm]	x = 0.2 Int. [%]	shift [ppm]	LW [ppm]
Li1	100	1022	37	51	1018	38	32	1024	36	14	1019	63	-	-	-
S1	0	-	-	21	920	209	25	921	167	23	829	152	0	-	-
S2	0	-	-	16	764	75	19	780	92	22	759	71	0	-	-
Li0.5*	0	-	-	9	736	28	18	742	28	31	736	24	45	732	24
	0	-	-	3	725	12	6	730	11	10	725	12	8	727	8
	0	-	-	-	-	-	-	-	-	-	-	-	47	740	111

* two subcomponents used to account for asymmetry.

NPD Neutron diffraction patterns of pristine and cycled LNMO-O-45 samples are shown in Fig. S4. The refinement parameters for the two pristine LNMO are shown in Tab. S2. The patterns of pristine LNMO, end of charge (EOC), end of discharge (EOD) and after 11 complete cycles greatly overlap without any additional features appearing. This underlines the structural stability of the spinel phase upon reversible delithiation and delithiation. It is noteworthy that also superstructural features reflecting the TM order are maintained upon cycling indicated by dashed vertical lines in the inset of Fig. S4. For the EOC sample, which was stopped towards end of complete delithiation, a shift of diffraction features to higher angle is observed which reflects the lattice shrinkage upon delithiation. It should be noted that this pattern was acquired at another beamline which results in different angular range, resolution and signal to noise ratio. The increased background for the cycled samples compared to pristine is result of scattering contribution of electrode additives.

XRD A close-up of the *operando* x-ray diffraction peak evolution in the range of $0.6<x<0.4$ can be seen in Fig. S5 in which the fading of one and the simultaneous emergence of a new peak reflects the biphasic transformation from Li1 to Li0.5 phase.

***Ex situ* NMR electrochemistry** The electrochemical cycling curves of each of the *ex situ* NMR samples stopped at distinct SoC are depicted in Fig. S6 and S7 for charge and

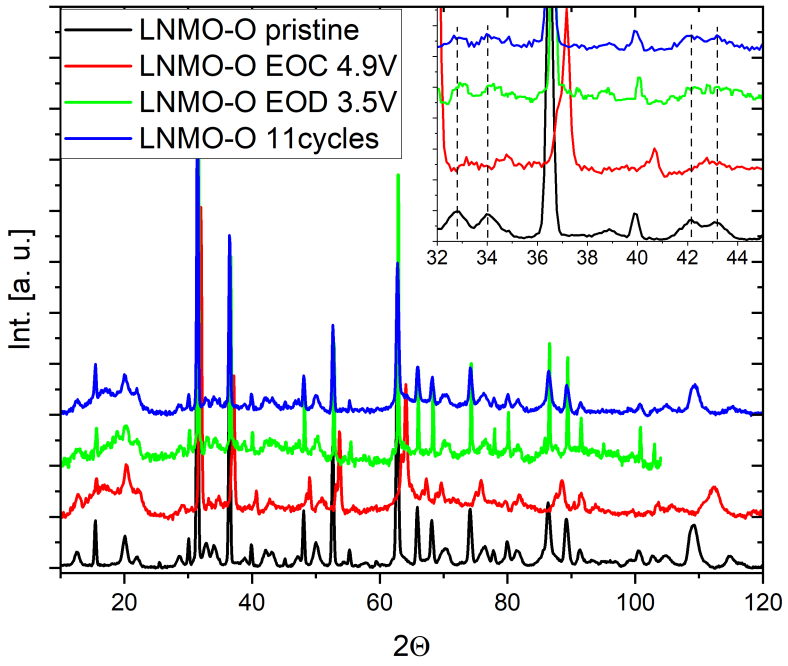

Figure S4: Neutron diffraction patterns of pristine, fully charged (EOC), after one complete cycle (EOD) and after 11 complete cycles. Inset shows the position of superstructural features by vertically dashed lines .

discharge, respectively.

Two distinct trends can be observed in the Fig S8. On the one hand the progressive transformation from thermodynamically stable Li1 prevalent until SoC x≈0.7 to Li0.5 phase upon delithiation represented by a decline in intensity of the former and a rise in intensity of the latter. Both of which have narrow spectral features and are not experiencing any significant chemical shift upon delithiation/ lithiation which can be attributed to the constant lattice parameter and the prevalence of a single Ni environment (either Ni^{2+} or Ni^{3+}) phase [S3]. On the other hand the intermediate species S1 and S2 which form during the biphasic transition of the Li1 to Li0.5 transformation and reach their relative maxima, contributing almost half of the overall intensity, at about x ≈ 0.5, are clearly distinct from the thermodynamic stable phases. Firstly and foremost, they are much broader which suggests

Table S2: Additional Rietveld refinement parameters of the neutron powder diffraction data.

Material	LNMO-O-48	LNMO-O-45
spacegroup	$P4_332$	$P4_332$
Fractional coordinates		
Mn/Ni x (12d)	0.125	0.125
Mn/Ni y (12d)	0.369(2)	0.381(4)
Mn/Ni z (12d)	0.873(2)	0.870(4)
Mn/Ni x,y,z (4b)	0.625	0.625
Li x,y,z (8c)	0.003(2)	0.005(4)
O1 x,y,z (8c)	0.3838(3)	0.3847(6)
O2 x (24e)	0.1505(3)	0.1497(8)
O2 y (24e)	0.8580(3)	0.8580(9)
O2 z (24e)	0.1242(4)	0.1247(7)
Occupancies *		
Mn (12d)	1.5	1.5
Ni/Mn (4b)	0.4826(7) / 0.0174(7)	0.454(3)/ 0.046(3)
Thermal movement Biso (Å^2)		
Mn (12d)	0.35(6)	0.5(2)
Ni/Mn (4b)	0.48(7)	0.7(2)
Li(8c)	1.0(1)	1.2(4)
O1(8c)	0.14(5)	0.4(2)
O2 (24e)	0.32(3)	0.55(7)
Quality indicators		
R_p	22.3	8.17
R_{wp}	16.5	8.72
R_e	1.56	1.26

* Sum of TM has been constrained
** Values without errors were fixed during the fit.

the presence of various Li environments, in this case a mix of Ni^{2+} and Ni^{3+}. Secondly, they experience a shift to lower ppm with increasing SoC, albeit much more pronounced for the S1 than for S2 which merges into the thermodynamically stable Li0.5 when approaching end of Ni^{3+} formation . This strong change in chemical shift of S1 may suggest a continuous, smooth transition between the main phases Li1 and Li0.5, with the presence of an intermediate lattice parameter (i.e. in S1 and S2), lithiation state, and TM oxidation state, reflecting an extended phase boundary region and varying Li solubility limit. The formation of such intermediate species during biphasic phase transition have been reported to be beneficial for rapid phase transition in LFP [S4, S5].

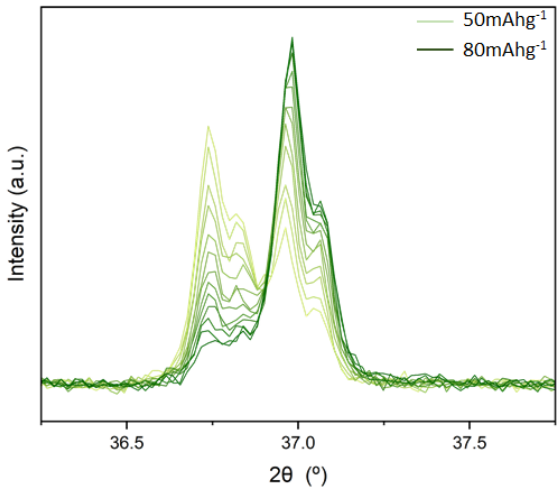

Figure S5: Evolution of *operando* XRD patterns of sample LNMO-O-45 in range of 50 (light green) to 80 mAh/g (dark green) ($\approx 0.6 \leq x \leq 0.4$) during charge, corresponding to the end of first lithiation plateau (Ni^{2+} to Ni^{3+} transformation).

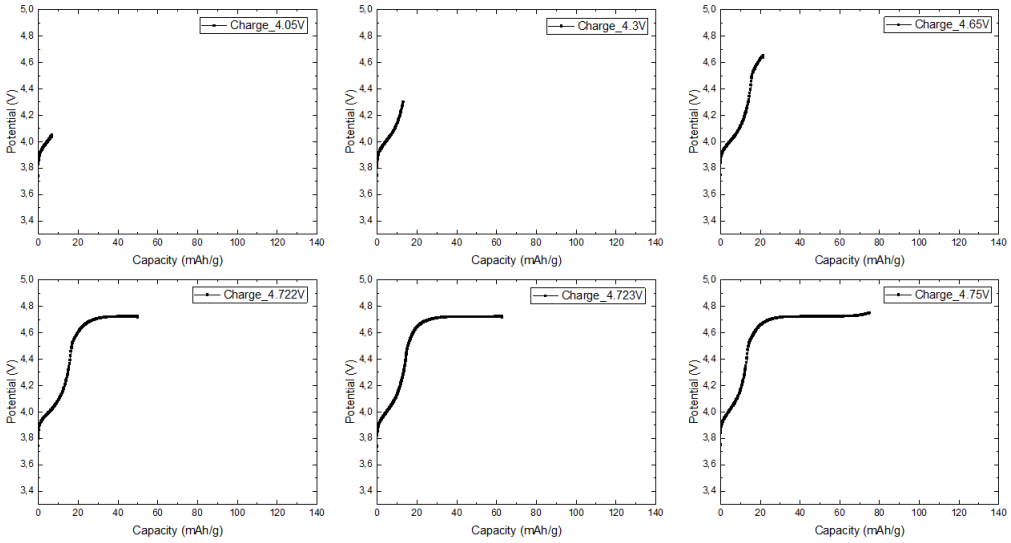

Figure S6: *Ex situ* electrochemistry during charge

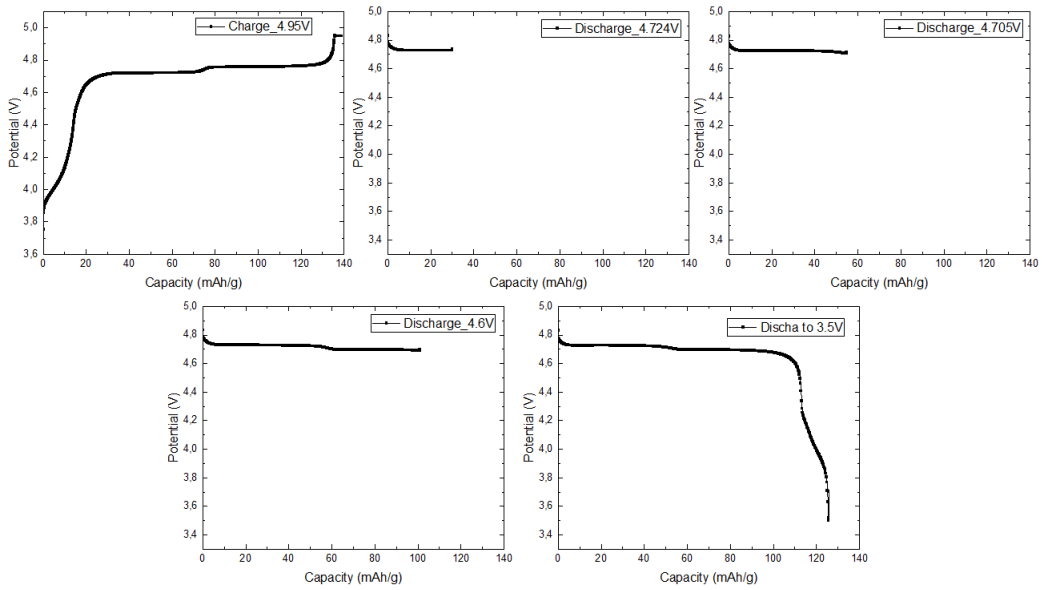

Figure S7: *Ex situ* electrochemistry during discharge

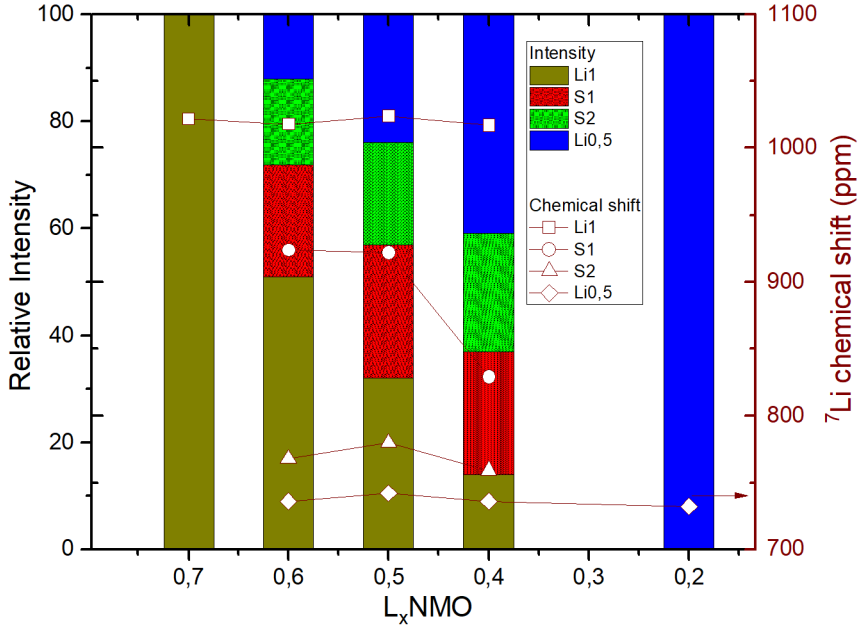

Figure S8: Relative peak intensities (bars) and chemical shift (hollow markers) of selected *ex situ* ^{7}Li NMR spectra at distinct SoC during charge and discharge.

References

(S1) Moorhead-Rosenberg, Z.; Chemelewski, K. R.; Goodenough, J. B.; Manthiram, A. Magnetic measurements as a viable tool to assess the relative degrees of cation ordering and Mn3+ content in doped LiMn1.5Ni0.5O4 spinel cathodes. *J. Mater. Chem. A* **2013**, *1*, 10745–10752.

(S2) Amdouni, N.; Zaghib, K.; Gendron, F.; Mauger, A.; Julien, C. Magnetic properties of LiNi0.5Mn1.5O4 spinels prepared by wet chemical methods. *Journal of Magnetism and Magnetic Materials* **2007**, *309*, 100–105.

(S3) Komatsu, H.; Arai, H.; Koyama, Y.; Sato, K.; Kato, T.; Yoshida, R.; Murayama, H.; Takahashi, I.; Orikasa, Y.; Fukuda, K.; Hirayama, T.; Ikuhara, Y.; Ukyo, Y.; Uchimoto, Y.; Ogumi, Z. Solid Solution Domains at Phase Transition Front of LixNi0.5Mn1.5O4. *Advanced Energy Materials* **2015**, *5*, 1500638, _eprint: https://onlinelibrary.wiley.com/doi/pdf/10.1002/aenm.201500638.

(S4) Liu, H.; Strobridge, F. C.; Borkiewicz, O. J.; Wiaderek, K. M.; Chapman, K. W.; Chupas, P. J.; Grey, C. P. Capturing metastable structures during high-rate cycling of LiFePO₄ nanoparticle electrodes. *Science* **2014**, *344*, 1252817.

(S5) Orikasa, Y.; Maeda, T.; Koyama, Y.; Murayama, H.; Fukuda, K.; Tanida, H.; Arai, H.; Matsubara, E.; Uchimoto, Y.; Ogumi, Z. Transient Phase Change in Two Phase Reaction between LiFePO4 and FePO4 under Battery Operation. *Chemistry of Materials* **2013**, *25*, 1032–1039.